A molecular dynamics analysis of the influence of iron corrosion products on the healing process of bitumen

Haiqin Xu [a,b], Yingxue Zou [a], Gordon Airey [b], Haopeng Wang [c], Hanyu Zhang [b], Shaopeng Wu [a,*], Anqi Chen [a,*]

[a] State Key Laboratory of Silicate Materials for Architectures, Wuhan University of Technology, Wuhan 430070, China;

[b] Nottingham Transportation Engineering Centre, Faculty of Engineering, University of Nottingham, University Park, Nottingham NG7 2RD, UK;

[c] Department of Civil and Environmental Engineering, University of Liverpool, Liverpool, L69 3BX, UK

* Correspondence author: wusp@whut.edu.cn (S. Wu), anqi.chen@whut.edu.cn (A. Chen).

ABSTRACT

Corrosion of iron materials in the asphalt concrete pavement occurs commonly when the bitumen film peels off, and the generation of corrosion products would affect the healing performance of bitumen. To identify the affection, this research focuses on the influence of iron corrosion products on the healing process of bitumen by molecular dynamics simulation. Firstly, bitumen model and iron corrosion products model were built. Then the healing systems of sandwich structure were constructed, and the simulated temperature were applied to reach equilibrium in the healing process with NVT ensemble (constant number of atoms, volume, and temperature). Dynamic movements of bitumen were characterized by appearance qualitatively. Healing rate of crack and healing rate of bitumen aggregation were held to evaluate the healing effect. Diffusion behaviors, internal force of motivation and interaction effect were also analyzed. The results indicate the duplicity of iron corrosion products in the healing process including the ease for bitumen climbing and the obstruction of bitumen movement. The comprehensive healing index demonstrated that iron corrosion products would reduce the healing degree, which was mainly caused by the obstruction effect and large internal stress generated by severe aggregation of bitumen in the limited space. From the perspective of crack closure and bitumen aggregation degree in the corrosion area, FeO healing systems were healed best, followed by Fe_3O_4, Fe_2O_3 and FeOOH. Furthermore, diffusion period of bitumen molecules on the surface of iron corrosion products during the healing process should be regarded as the important period affecting healing.

33

35

1 Introduction

Highways are always considered as the most important systems in the transportation infrastructures, where asphalt concretes are widely applied on the highway due to its marked service characteristics including comfort driving, low noise, outstanding skid resistance, simplicity of maintenance [1–3]. More than 90% roads of Europe are constructed by asphalt concrete and its mileage in China is in excess of 1.2 million kilometers [4–6]. However, it should be admitted that asphalt concrete pavement has been constantly exposed to the damage of heavy ultraviolet light, moist climate and continuous loading since it was built [7–9]. The damages will oxidize and harden the bitumen and then result in various deteriorations [10,11]. According to the official report by the Ministry of Transport of the People's Republic of China, the accumulated maintenance road length has exceeded 535.03 kilometers by 2022, accounting for 99.9 % of total road length [12]. Once the damages are not maintained and repaired in time, it will cause immeasurable damage to pavement safety and transportation. Therefore, the development of advanced and effective maintenance technology has become the emergency task.

The current advanced maintenance technology include encapsulation technology, microwave heating technology and induction heating technology, which can accelerate the healing of cracks by reducing the viscosity and enhancing the fluidity of bitumen [13–15]. Among these technologies, induction heating technology is considered the renewable and sustainable method with the advantages of high efficiency and cleaner production, and would be potential to become to a common maintenance method soon. The method was developed on excellent magnetic conductivity of steel products like steel wool fibers, steel shaves and steel grits [16]. The asphalt concrete with the steel products can be induced-heated firstly and then flow to heal the microcrack generated by aging, hardening and loading under variable magnetic field [17–19]. However, while recognizing the advanced and suitable characteristics of induction heating technology, it can't be ignored that the activity of iron materials in steel products lead to their easy reaction and action with the environment, especially the potential

63   situation of direct exposure of metal materials [20].

64   Steel products consist of a large amount of iron and a small amount of carbon, where the

65   reactivity of iron would make it susceptible to severe corrosion while it is constantly exposed

66   to environment and loading. Suda et al and Duffo et al have investigated the corrosion of steel

67   bar in concrete, and the results show that even if the iron material is wrapped, it may still be

68   subjected to erosion, and the erosion products of which consist of the crystal substances like

69   magnetite, goethite, lepidocrocite, meanwhile the corrosion products are in a state of changing

70   composition and related to the environment [21,22]. In generally, the steel products in the

71   asphalt concrete would be considered being wrapped in the bitumen during the service life.

72   Though asphalt concrete was exposed to extreme environment and intense loading, the steel

73   products were also hard to get damage, because the effect of environment can hardly penetrate

74   the wrapped bitumen film and the loading can't strip bitumen from its surface [23]. However,

75   once cracks occur in asphalt concrete, the bitumen wrapped around steel products will peel off

76   and the cross section of the steel products would be exposed to the environment directly.

77   Furthermore, it is hard for the roads agency to judge the time to fix the crack, which would

78   worsen the erosion. Then, the deposits of generated corrosion products on the interface of

79   asphalt concrete would obstruct diffusion between bitumen and bitumen, and finally affect the

80   healing performance of induction heating technology [24]. In addition, the corrosion process

81   will make the oxide layer on the steel products grow, thus generating internal stress. If this

82   corrosion process is allowed to continue, it will lead to the situation that the old cracks have

83   not been closed and new cracks have been produced [25]. Therefore, it is necessary to clarify

84   the influence of corrosion products of steel products on healing effect of bitumen for the better

85   maintenance effect.

86   Molecular Dynamics (MD) simulation is a suitable method for investigating the

87   movements and dislocations of nanoparticles [26]. It describes the motions and positions of

88   atoms based on Newton's second law. Empirical force-field equations are used to describe

89   interatomic forces, electron interactions, and other energies during the simulation. The MD

90   method can describe various scales and indicators, such as the change in energy of the proton

91   system, mean-square displacement of the atomic system, and adsorption state between atoms

92   [27,28]. These indicators are physical quantities that have been demonstrated to be describable

93   by MD, both theoretically and experimentally [29–31]. Molecular dynamic (MD) simulation

94   would be advantageous compared with the phenomenological method: it is not limited by

95   experimental methods or specimen preparation conditions and can effectively address the

96   shortcomings of macroscopic scales. Several studies by MD simulation have been carried out

97   to investigate the healing properties of bitumen. Bhasin et al used MD simulation to investigate

98   the mechanism of self-healing of bitumen and demonstrated the correlation of chain length and

99   chain branching to self-diffusivity of bitumen molecules [32]. Sun et al have conducted

100   molecular dynamics simulation to evaluate the hypothesis of healing mechanism and evaluate

101   the self-healing capability of virgin and SBS modified asphalt binder by introducing the micro-

102   crack model [33,34]. Qu et al and Zhang et al focused on the behavior characteristics of fractions

103   of bitumen during the healing process [35,36]. The influence of the addition on the healing

104   performance of bitumen have been also investigated, which includes waste vegetable oil,

105   soybean-oil, graphene, iron oxide, nanomaterials and rubbers [37–42]. Furthermore, the

106   investigations related to bitumen and iron oxide have also been conducted, but it mainly

107   focuses on the interaction effect and the adhesion property between bitumen and iron oxide

108   [43,44]. Therefore, it can be found that the current research mainly focused on the healing

109   process and healing mechanism of bitumen, the materials that would be beneficial to the

110   healing property, and the interaction effect and the adhesion property between bitumen and

111   iron oxide, while few work has been conducted to investigate the effect of diffusion-blocking

112   substances like iron corrosion products on self-healing properties of bitumen at the molecular

113   scale. In general, it is necessity for understanding the influence of iron corrosion products on

114   the healing of bitumen at atomic scale, which would be investigated in the study.

115   The main purpose of this research is to investigate the influence of iron corrosion products

116   on the healing process of bitumen by molecular dynamics simulations. The bitumen model and

117   iron corrosion products model including Fe_2O_3, Fe_3O_4, FeO and $FeOOH$ were built. Then the

118   healing systems were constructed, and the simulated temperature were applied to reach

119   equilibrium in the healing process. The dynamic movements of bitumen were characterized,

120   and healing rate indexes of crack closure, healing rate of bitumen aggregation and their

121   comprehensive indexes were held to evaluate the healing effect. Diffusion behavior of the

122   bitumen molecules and the internal force motivating bitumen molecules in the healing systems

123 were evaluated. Eventually, interaction effects between bitumen and iron corrosion products

124 were obtained and analyzed.

125

126 2 Molecular dynamic simulation models and simulation details

127 *2.1 Bitumen*

128   The bitumen molecular model was built based on the AAA-1 bitumen model proposed by

129 Li and Greenfield. As shown in the Figure 1, it has 12 components and its characteristics were

130 proved closer to experimental data [45]. Materials studio software was used for the

131 establishment and thermodynamic properties calculation for the models. 12-components

132 molecular models were built in 3D Atomistic. Condensed-phase optimized molecular

133 potentials for atomistic simulation studies (COMPASS) was selected as the force field, which

134 can predict and calculate the structure and thermophysical properties of common inorganic

135 and organic system over a large temperature and pressure range [46]. The model was

136 constructed with the following step: Firstly, the model was constructed by Amorphous Cell

137 tools with an initial density of 0.1 g/cm^3 under the three-dimensional cycle condition. The

138 geometric optimization with 5000 iterations was followed to eliminate unreasonable

139 configurations in the model, leveling off the energy of the molecule to reach minimum energy.

140 Then, Forcite tools was used to reach dynamic equilibrium for the stable structure and density,

141 where a canonical ensemble (NVT, constant molecule number, model volume, and temperature)

142 with 298 K, 1 fs time step for 100 ps and an isothermal-isobaric ensemble (NPT, constant atomic

143 number, pressure, and temperature) with 298 K and 1.0 atm were conducted successively. The

144 temperature and pressure of the block were controlled by Andersen barostat and Nose-

145 Hoover-Langevin thermostat. Moreover, the Ewald with the accuracy of 0.001 kcal/mol and

146 Atom-based with the cutoff distance of 15.5 Å are assigned as the Electrostatic and van der

147 Waals summation method. Finally, the models have been established for further performance

148 prediction and analysis in terms of thermodynamics parameters, structural characteristics, and

149 dynamic behaviors. The rationality and reality of this model have been proved in our previous
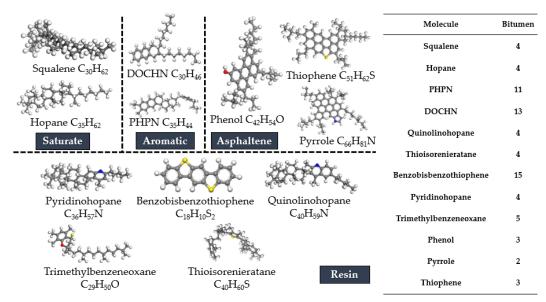
150 studies [47].

151

Molecule	Bitumen
Squalene	4
Hopane	4
PHPN	11
DOCHN	13
Quinolinohopane	4
Thioisorenieratane	4
Benzobisbenzothiophene	15
Pyridinohopane	4
Trimethylbenzeneoxane	5
Phenol	3
Pyrrole	2
Thiophene	3

Figure 1. 12-components molecules models and molecular compositions of bitumen

2.2 Iron corrosion products

The iron products will be corroded in the environment with air and water, and the corrosion process is a dynamic process, whose products will be constantly transformed. Commonly, the corrosion products are mainly composed of Fe_2O_3, Fe_3O_4, FeO and FeOOH [20,48], therefore α-Fe_2O_3 (Hematite), Fe_3O_4 (Magnetite), FeO and α-FeOOH (Geothite) were selected as the iron corrosion products in this research. The unit cell constants and unit cell structure models of Fe_2O_3, Fe_3O_4, FeO and FeOOH are shown in Table 1 [49–52]. The models of iron corrosion products were also established by Materials studio software and the steps were as follows: Firstly, the lattice was converted into an orthorhombic lattice. The plane's crystal face was sliced using the Cleave Surface tool with specific Miller index where (1 0 0) was for Fe_3O_4, FeO, (1 1 0) was for Fe_2O_3 and (0 1 0) was for FeOOH. The reason for the adoption of crystallographic surface plane was that these crystallographic surfaces showed the least lattice mismatch shown in the previous research that adsorption and diffusion of organic molecules happened on iron oxide surfaces, meanwhile the oxygen ions were full bulk-coordination on the surfaces [53–55]. Then, before performing energy reduction on the unit cell structure, it was necessary to ensure that the COMPASS force field of each atom in the iron corrosion products unit cell was accurately assigned and that chemical linkages between atoms were deleted, which can describe the different valence states of iron atoms. Finally, the optimized unit cell model was enlarged to a supercell model with similar size and volume to eliminate the size

174   effect and a certain lattice same to bitumen model was added to the unit cell model. The

175   establishment of the supercell model of Fe_2O_3 molecule was as an example shown in Figure 2.

176   The supercell models of iron corrosion products and their parameters are also shown, where

177   there are two sizes of each iron corrosion products were established to investigate the influence

178   of iron corrosion products volume on the healing performance.

179

180   Table 1. Unit cell of iron corrosion products and lattice parameters

Corrosion Products	Unit cell structure	Unit cell constants	
Fe_2O_3		a = 5.035 Å, b = 5.035 Å, c = 13.720 Å	α= 90 °, β = 90 °, γ=120 °
Fe_3O_4		a = 8.394 Å, b = 8.394 Å, c= 8.394 Å	α=90 °, β =90 °, γ=90 °
FeO		a = 4.332 Å, b = 4.332 Å, c= 4.332 Å	α=90 °, β =90 °, γ=90 °
FeOOH		a = 4.604 Å, b = 9.951 Å, c = 3.019 Å	α=90 °, β =90 °, γ=90 °

181

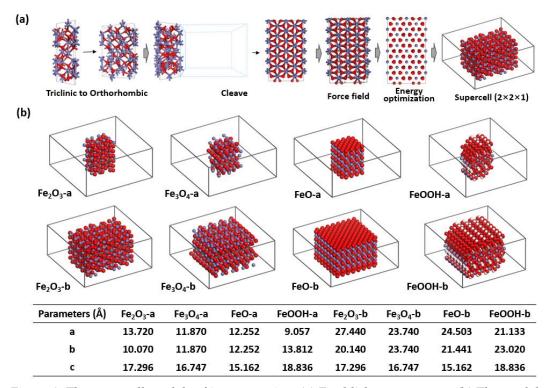| Parameters (Å)	Fe₂O₃-a	Fe₃O₄-a	FeO-a	FeOOH-a	Fe₂O₃-b	Fe₃O₄-b	FeO-b	FeOOH-b
a	13.720	11.870	12.252	9.057	27.440	23.740	24.503	21.133
b	10.070	11.870	12.252	13.812	20.140	23.740	21.441	23.020
c	17.296	16.747	15.162	18.836	17.296	16.747	15.162	18.836

Figure 2. The supercell models of iron corrosion: (a) Establishment process; (b) The models and the size parameters

2.3 Healing systems

The healing systems were developed by the Materials studio software's Build Layers tools with the obtained bitumen models and iron corrosion products models. Iron corrosion products healing systems have triple layers: a bitumen layer as the foundation, an iron corrosion products layer as the middle layer, and another bitumen layer on top of the iron corrosion products layer. Bitumen healing systems were constructed by bitumen layer, vacuum layer and another bitumen layer. The healing systems are shown in Figure 3: Bitumen healing system and iron corrosion products healing systems including group-a (Fe₂O₃-a, Fe₃O₄-a, FeO-a and FeOOH-a) and group-b (Fe₂O₃-b, Fe₃O₄-b, FeO-b and FeOOH-b).
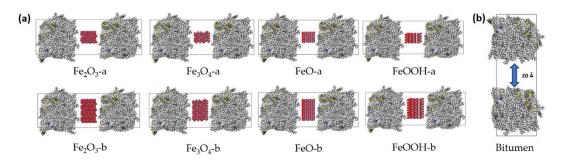

Figure 3 The model of healing systems: (a) Iron corrosion products

198   ; (b) Bitumen

199

200   *2.4 Simulation details*

201   In this study, a classical molecular dynamics code: the large-scale atomic/molecular

202   massively parallel simulator (LAMMPS) was used to perform the simulation. The polymer

203   consistent force field (PCFF) was chosen for bitumen simulation, which has been validated to

204   describe the organic, inorganic, and organic–inorganic interface systems. The force field is an

205   empirical expression of the potential energy surface, and the total energy of the molecules is

206   the sum of kinetic energy and potential energy. Moreover, the total potential energy is

207   composed of bond angle bending potential energy, bond stretching potential energy, dihedral

208   angle twisting potential energy, off-plane vibration potential energy, Waals potential energy

209   and Coulomb electrostatic potential energy, shown in Equations (1).

$$E_{\text{potential}} = \sum_{\text{cross}} E(b,\theta,\varphi) + \sum_{\text{bond}} E_b(b) + \sum_{\text{torsion}} E_\varphi(\varphi)$$
$$+ \sum_{\text{angle}} E_\theta(\theta) + \sum_{\text{inversion}} E_x(x) + E_{ele} + E_{vdw} \tag{1}$$

210   where $E_{\text{potential}}$ is the total energy; $\sum_{\text{cross}} E(b,\theta,\varphi)$ represents the cross term potential

211   energy; $\sum_{\text{bond}} E_b(b)$ is the bond stretching potential energy; $\sum_{\text{torsion}} E_\varphi(\varphi)$ is the dihedral

212   angle twisting potential energy; $\sum_{\text{angle}} E_\theta(\theta)$ is the bond angle potential energy;

213    $\sum_{\text{inversion}} E_x(x)$ is the off-plane vibration potential energy; E_{ele} is the Coulomb electrostatic

214   potential energy and E_{vdw} is the Waals potential energy. The interaction between bitumen and

215   corrosion products can be described by the 6/9 Lennard–Jones potential (Sun 1998), as shown

216   in Equations (2)-(3). The LJ 9-6 and Coulombic interactions are truncated to 10 Å and 8 Å.

$$E_{\text{ele}} = \sum_{i>j} \frac{q_i q_j}{r_{ij}} \tag{2}$$

$$E_{vdw} = \sum \varepsilon_{ij} \left[2 \left(\frac{r_{ij}^0}{r_{ij}} \right)^9 - 3 \left(\frac{r_{ij}^0}{r_{ij}} \right)^6 \right] \tag{3}$$

217   where q_i and q_j are the charges of atomic i and j; r_{ij} is the distance of atomic i and j

218   and ε_{ij} is the well depth of atomic i and j, respectively.

219   Each simulation process consists primarily of the following steps: (1) Energy minimization

220   was used to remove any potential energy excess that existed in the initial configuration. (2) The

221   healing system was then relaxed using NVT (constant number of atoms, volume, and

222   temperature) ensemble at 373 K for 1000 ps, which was the common healing temperature used

223   in the induction heating [24]. Simultaneously, the iron corrosion products layer in each model

224   was fixed and each valence state of iron atom was arranged to the corrosion products to

225   precisely calculate the indicators of   healing system.

226

227   3 Evaluation indexes

228   *3.1 Healing rate indexes*

229   3.1.1 Healing rate of crack

230   The closure of cracks is considered as a sign of healing of bitumen, but it is hard to calculate

231   the accurate volume of crack during the simulation. So the difference value of centroid position

232   between bitumen molecules are used to propose the healing rate of crack as shown in Figure 4

233   and its calculation is accorded to Equation (4) and (5):

$$\Delta L = |Z_{bitumen1} - Z_{bitumen2}| \tag{4}$$

$$H_1 = 1 - \frac{\Delta L_{iron} - \Delta L_{bitumen}}{\Delta L_{bitumen}} \times 100\% \tag{5}$$

234   Where ΔL represents the absolute value of the difference value of centroid position between

235   bitumen layers in the healing systems; $Z_{bitumen1}$ represents Z coordinate of centroid position

236   of one bitumen layer in the healing systems; $Z_{bitumen2}$ represents Z coordinate of centroid

237   position of the other bitumen layer in the healing systems; ΔL_{iron} represents the average value

238   of difference value of centroid position between bitumen layers in the iron corrosion products

239   healing systems from 900 ps to 1000 ps; $L_{bitumen}$ represents the average value of difference

240   value of centroid position between bitumen layers in the bitumen healing systems from 900 ps

241   to 1000 ps; H_1 represents the healing rate of crack, and greater value indicates the closer of the

242   bitumen combination in this system compared to that of bitumen healing systems, as well as
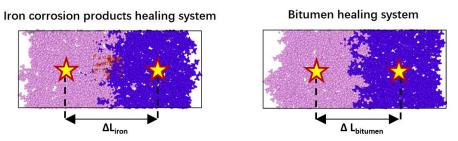
243   that the better the cracks are closed.

244

245   Figure 4 Difference value of centroid position between bitumen in the healing systems

246

247 3.1.2 Healing rate of bitumen aggregation

248   Healing rate of bitumen aggregation is held to evaluate the diffusion of bitumen molecules

249 after the cracks are closed. Firstly, the relative concentration of bitumen molecules should be

250 obtained. It was computed as the ratio of the atom number in the unit volume perpendicular

251 to the axis to the atom number in the unit volume of the amorphous unit. The three-

252 dimensional periodic system should be partitioned into evenly spaced plates in the interfacial

253 system. The distribution of atomic density in each plate was then computed to give the overall

254 structure's relative concentration distribution. As shown in Figure 5, iron corrosion products

255 healing systems are divided into three parts: free area 1, free area 2 and corrosion area; the free

256 area is also separated in bitumen healing systems. The standard of demarcation is the position

257 of iron corrosion products and the peak of relative concentration of bitumen. The average value

258 of relative concentration of bitumen in free area of bitumen healing systems should calculated

259 firstly as the reference. Then the average value of relative concentration of bitumen in the

260 selected area of iron corrosion products healing systems should be calculated respectively.

261 Healing rate of bitumen aggregation can be calculated as Equation (5)-(9):

$$M_0 = \frac{R_0}{V_0 - V_{iron}} \tag{5}$$

$$M_f = \frac{\left(\frac{R_1}{V_1} + \frac{R_2}{V_2}\right)}{2} \tag{6}$$

$$M_b = \frac{R_3}{V_3} \tag{7}$$

$$H_{2a} = \frac{M_0}{M_b} \times 100\% \tag{8}$$

$$H_{2b} = \frac{M_f}{M_b} \times 100\% \tag{9}$$

262 Where M_0 represents the relative concentration per unit volume of bitumen in corrosion area

263 of iron corrosion products healing systems; R_0 represents the sum of relative concentration of

264 bitumen in corrosion area of iron corrosion products healing systems; V_0 represents the

265 volume of corrosion area of iron corrosion products healing systems; V_{iron} represents the

266 volume of iron corrosion products; M_f represents the relative concentration per unit volume

267 of bitumen in free area of iron corrosion products healing systems; R_1 and R_2 represent the

268 sum of relative concentration of bitumen in free area of iron corrosion products healing systems

269   respectively; V_1 and V_2 represent the volume of free area 1 and free area 2 of iron corrosion

270   products healing systems respectively; M_b represents the relative concentration per unit

271   volume of bitumen in free area of bitumen healing systems; R_3 represents the sum of relative

272   concentration of bitumen in free area of bitumen healing systems; V_3 represent the volume of

273   free area of bitumen healing systems; H_{2a} and H_{2b} represent the healing rate of bitumen

274   aggregation in corrosion area and free area of iron corrosion products healing systems, and

275   greater value indicates serve bitumen aggregation in this area of iron corrosion products

276   healing systems compared to that of bitumen healing system.

277
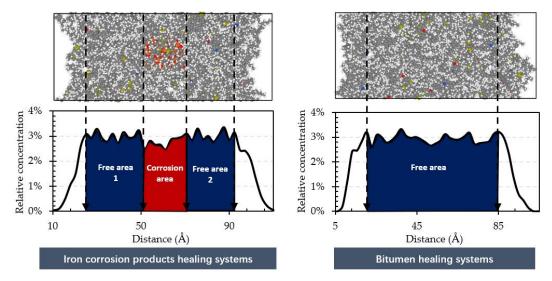
278   Figure 5 Schematic diagram of relative concentration of bitumen in the healing systems

279

280   *3.2 Diffusion and interaction indexes*

281   3.2.1 Mean square displacement and diffusion coefficient

282   The core regulation of diffusion phenomena was the movements of atoms in three-

283   dimension space, which was vital to analyze the interaction between bitumen and corrosion

284   products. However, due to the enormous number of atoms in the interface system, detecting

285   each atom's motion trajectory is difficult. As a result, mathematical statistics method was held

286   to describe the regularity of particle movement. The most commonly used indicator was mean

287   square displacement (MSD), which would be represented and calculated by Equation (10):

$$MSD(t) = (|r_i(t) - r_i(0)|^2) \qquad (10)$$

288   Where, $MSD(t)$ indicated as the mean value of all atoms' movement positions in the molecular

289   system, $r_i(0)$ indicated the original position of particle i, and $r_i(t)$ indicated the position of

290   particle i at the time of t.

291   Diffusion coefficient, for the measurement of the molecule's capacity for diffusion, rate at

292 which a quantity diffuses per unit area while the concentration gradient is the same unit.

293 MSD had a linear relationship with time and was correlated with the diffusion coefficient after

294 diffusion relaxation process. After this period, the linear slope of the MSD curve might be used

295 to compute the diffusion coefficient of the contact system, as indicated by Equation (11):

$$D = \frac{1}{6N} \lim_{t \to \infty} \frac{d}{dt} \sum_{i=1}^{N} (|r_i(t) - r_i(0)|^2) \approx \frac{1}{6} K_{MSD} \tag{11}$$

296 Where, the diffusion coefficient was recorded as D in the interface system, N indicated the

297 whole number of molecules in the interface system, and the differential term was equal to the

298 linear slope of the interface system's MSD curve, K_{MSD} was equal to the linear slope of the

299 interface system's MSD curve.

300

301 3.2.2 Interaction energy and debonding energy

302   Interaction energy could be used to evaluate the stability of the selected molecules. The

303 greater its absolute value, the more interaction there was between the selected molecules. When

304 the value of interaction was zero or positive, adsorption was minor or non-existent. Its

305 calculation formula was shown in Equation (12):

$$E_{inter} = (E_{pe1} + E_{pe2} + \cdots + E_{pei}) - E_{pe-total} \tag{12}$$

306 Where E_{inter} represented the interaction energy between the selected molecules, $E_{pe-total}$

307 represented that the total potential energy of the selected molecules in a steady state, E_{pei}

308 represented the total potential energy of every component of the selected molecules

309 individually.

310   Debonding energy is defined as the energy for the separation of the bitumen in the healing

311 systems, which can be calculated by Equation (13):

$$E_{debonding} = E_{inter2} - E_{inter1} \tag{13}$$

312 Where $E_{debonding}$ is the debonding energy; E_{inter1} is the interaction energy between bitumen

313 and bitumen in the iron corrosion products healing systems; E_{inter2} is the interaction energy

314 between bitumen and iron corrosion products in the iron corrosion products healing systems.

315   Another parameter used in this study to further define the debonding property was the

316 Energy Ratio, which was computed as the ratio of the interaction energy between bitumen of

317   bitumen healing systems to the debonding energy of iron corrosion products healing systems,

318   as calculated as Equation (14) [56]:

$$ER = \frac{E_{inter3}}{E_{debonding}} \times 100\% \tag{14}$$

319   Where ER is the Energy Ratio; E_{inter3} is the interaction energy between bitumen and bitumen

320   in the bitumen healing systems; $E_{debonding}$ is the debonding energy.

321

322   4 Results and discussion

323   *4.1 Dynamic movement and healing rate of crack*

324   Figure 6 shows the healing process of bitumen in the different healing systems where the

325   snapshots of the healing systems at 5 ps, 25 ps, 50 ps, 500 ps and 1000 ps are selected. It can be

326   found in the bitumen healing systems that the bitumen molecules would get close firstly, and

327   then the molecules would seize each other to reduce the vacuum area. Finally, the crack was

328   filled with bitumen completely and the bitumen molecules were keeping diffusion. Similarly,

329   the bitumen molecules in the iron corrosion products healing systems would also get touch

330   firstly, caputure the iron corrosion products, and finally swallow the iron corrosion products.

331   In this process, it can be observed that the bitumen molecules would climb on the surface of

332   iron corrosion products firstly and then cover the iron corrosion products completely, rather

333   than fillling the vacuum area directly like that in bitumen healing systems. It was caused by the

334   absorption force generated by iron corrosion products that was obvious larager than that of

335   vaccum, therefore the iron corrosion products could drag the bitumen molecules forwards to

336   its position. In addition, during the absorption process, the aggregation degree of bitumen on

337   the iron corrosion products were quite different. It is clearly that the aggregation of bitumen

338   on Fe_2O_3, Fe_3O_4 and FeO were more severe than that of FeOOH at 50 ps. The volume of iron

339   corrosion products would also affect the diffusion of bitumen molecules: at 1000 ps, the iron

340   corrosion products of Fe_2O_3-b, Fe_3O_4-b, FeO-b and FeOOH-b systems were more obvious to

341   observe than Fe_2O_3-a, Fe_3O_4-a, FeO-a and FeOOH-a systems. Larger iron corrosion products

342   volume means that there are few space for the bitumen molecules to move, which results in

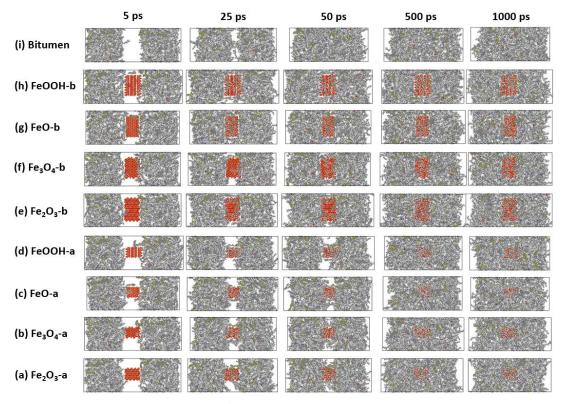343   that only small molecules are accessible to diffusion while marcomolecules were blocked out

344   the space.

345

346
347   Figure 6 Trajectories of bitumen in the healing systems at 373 K
348

349   Figure 7 shows the changing of ΔL of bitumen molecules in different healing systems. It

350 can be found from Figure 7 (a) that the ΔL curve of bitumen healing systems can be divided

351 into two parts (rapidly decrement and equilibrium): first, it would decrease to the equilibrium

352 value straightly, and then it would keep the equilibrium value dynamically. The addition of

353 iron corrosion products into the healing systems made the crack closure process dissimilarly.

354 The ΔL curves of iron corrosion products healing systems can be divided into three parts:

355 rapidly decrement, slowly decrement and equilibrium. It is clearly that the rapidly decrement

356 part were affected significantly and rapidly crack closure was retarded, which was caused by

357 the obstruction of iron corrosion products. The slowly decrement part of group-a and group-b

358 of iron corrosion products healing systems were affected by the volume of iron corrosion

359 products obviously. The bitumen molecules could differ through the side surface of iron

360 corrosion products in group-a while the bitumen molecules only diffused on the top and

361 bottom surface of iron corrosion products in group-b and could hardly catch the molecules in

362 the other side. Therefore, the healing process of group-a was controlled by movements of

363 bitumen and attraction of iron corrosion products collectively while that of group-b was

364   controlled by attraction of iron corrosion products mainly. Figure 7 (b) shows ΔL of different

365   healing systems at equilibrium. It can be found that ΔL of bitumen system was the least, which

366   was the results of free diffusion without the obstruction and attraction of iron corrosion

367   products. ΔL of group-a was obviously less than that of group-b, also indicating that the

368   obstruction and attraction were affected by the volume changing of iron corrosion products.

369   With healing system of bitumen regarded as none iron corrosion products, the influence of the

370   volume of iron corrosion products could be analyzed by linear fitting and the slope can reflect

371   the sensitivity. The results of slope indicate that healing system of FeOOH was the most

372   sensitive to iron corrosion products volume, followed by Fe_2O_3, Fe_3O_4, and FeO.

373
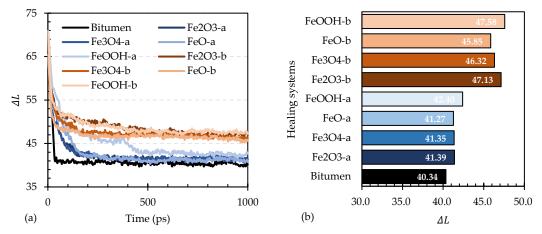
374   Figure 7 Dynamic movements of bitumen molecules: (a) ΔL of different healing systems with
375   the simulated time; (b) ΔL of different healing systems at equilibrium

376

377   Figure 8 shows the healing rate of crack in the healing systems, which was calculated

378   according to Equation (4) in section 3.1.1 with ΔL of bitumen healing system as the reference.

379   It means that the crack closure in the bitumen healing systems was considered completely, It

380   can be found that H_1 of group-a of iron corrosion products healing systems were obviously

381   larger than H_1 of group-b of iron corrosion products healing systems. It indicates that a larger

382   volume of iron corrosion products would weaken the crack closing of bitumen molecules. The

383   reason is that the larger obstruction area made bitumen molecules unable to diffuse freely.

384   Inside the group-a and group-b of iron corrosion products healing systems, H_1 both show the

385   regularity that FeO> Fe_3O_4> Fe_2O_3> FeOOH, which was consistent with the results of Figure 7

386   (b). In addition, the difference values of H_1 between different healing systems were more
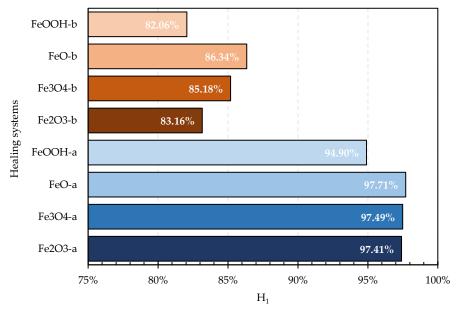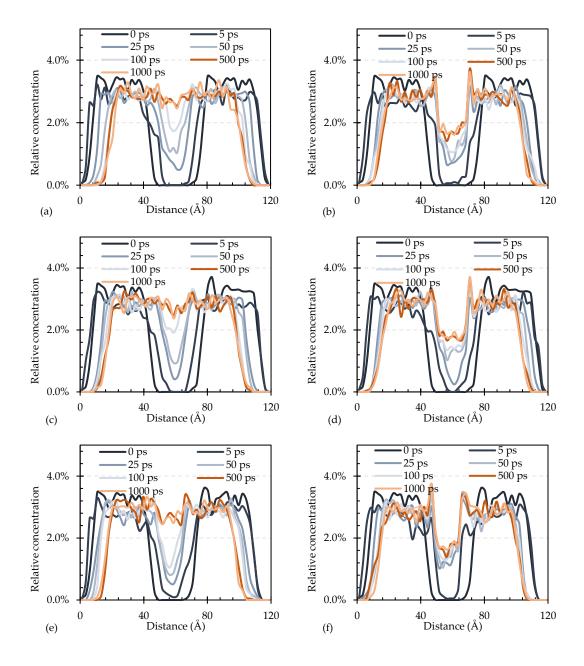
387 obvious in group-b of iron corrosion products healing systems. It demonstrates that the

388 increment of iron corrosion products volume will enhance the difference of crack closing.

389

390
391 Figure 8 Healing rate of crack in the healing systems

392

393 *4.2 Healing rate of bitumen aggregation*

394 The closure of cracks cannot represent healing of bitumen completely. In the healing

395 process, bitumen molecules would continue diffusion to recover strength after the cracks are

396 closed. Therefore, another index of bitumen aggregation in the healing systems were held for

397 the evaluation. Relative concentration of bitumen in the healing systems should be

398 demonstrated firstly, which is shown in Figure 9, representing the aggregation degree of

399 bitumen in the healing systems. It can be found that the relative concentration of the bitumen

400 in the healing systems shows bimodal shape initially: there were few bitumen molecules in the

401 middle area. Within 100 ps of simulated time, the bottom of recess changed from plate shape

402 to sharp shape gradually, which indicates that the bitumen molecules would move to the crack

403 area gradually and the center of middle area was the hardest area of arrive. Meanwhile it is

404 observed that the relative concentration of bitumen on both sides of the healing systems

405 decreased. In group-a, the relative concentration of bitumen in the middle would slowly

406 increase approaching to that of both sides, while the relative concentration of bitumen in the

407 middle of group-b was still less than that of both sides obviously. At 1000 ps of simulated time,

408   the relative concentration of bitumen in group-b still shows bimodal shape while that in group-

409   a have changed to the plate shape. Moreover, it can be also found that the bitumen molecules

410   contracted to the middle, and the overall volume decreased. Figure 9 (j) shows the average

411   value of relative concentration of bitumen molecules in the middle area. The relative

412   concentration of bitumen in bitumen healing systems was the largest, and the order of relative

413   concentration of bitumen that $FeO > Fe_3O_4 > Fe_2O_3 > FeOOH$ were found in group-a and $FeO >$

414    $Fe_3O_4 > FeOOH > Fe_2O_3$ were found in group-b.

415
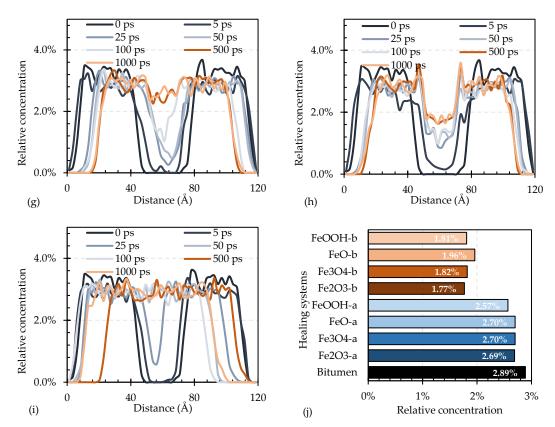
Figure 9 Relative concentration of bitumen in the healing systems at 373 K: (a) Fe_2O_3-a; (b) Fe_2O_3-b; (c) Fe_3O_4-a; (d) Fe_3O_4-b; (e) FeO-a;(f) FeO-b;(g) FeOOH-a;(h) FeOOH-b; (i) Bitumen; (j) Average value in the middle area

Based on the results of Figure 9, the healing rate of bitumen aggregation in the healing systems was calculated according to Equation (5)-(9) with the value of bitumen healing systems as the reference. It means that bitumen aggregation degree in bitumen healing systems was considered as 100%. It can be found in Figure 10 (a) that relative concentration of bitumen in the healing systems was ordered as FeO> Fe_3O_4> Fe_2O_3> FeOOH, which indicates that the bitumen in the middle area of FeO healing systems possessed the most serve aggregation degree. The H_{2a} value in FeO-b healing systems has exceeded 100% demonstrating that the addition of sufficient volume of FeO resulted in closer combination of bitumen molecules in the corrosion area. The result also indicated that the few movements space in the corrosion area of group-b wouldn't reduce the bitumen aggregation degree. Conversely, an influx of more small molecules might intensify the aggregation degree. Figure 10 (b) shows the healing rate bitumen aggregation of free area in the healing systems. It can be observed that the values all have exceeded 100%, which was caused by the insufficient aggregation in corrosion area and the occupation of iron corrosion products.
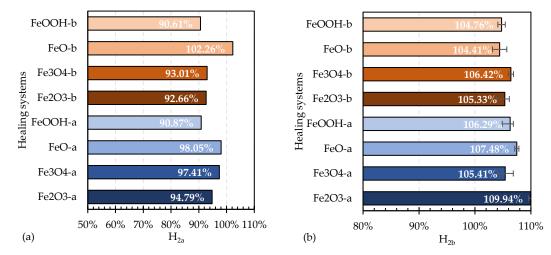
434

To combine the healing rate of crack and healing rate of bitumen aggregation, a comprehensive healing rate (H_3) of bitumen in the healing systems were held, which was defined as the product of healing rate of crack (H_1) and healing rate of bitumen aggregation (H_{2a}). The index combines the evaluation of crack closure and intrinsic diffusion of the bitumen in the healing systems. As shown in Figure 11, H_3 of the healing systems demonstrated the regularity that FeO> Fe_3O_4> Fe_2O_3> FeOOH in both group-a and group-b. The results indicate that the bitumen in the FeO healing systems could be healed best while that of FeOOH healing systems was the worst. The existence of FeO can make the bitumen molecules closer to each other and attract more bitumen molecules around the FeO crystals to realize better healing effect. It can be also found that the healing rate of group-a was obviously larger than that of group-b, which was mainly caused by the difference of iron corrosion products volume.
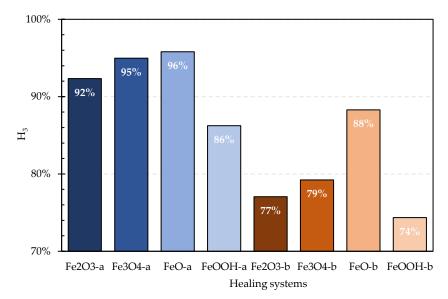
Figure 11 Comprehensive healing rate of bitumen in the healing systems

4.3 Diffusion behavior of bitumen in the healing systems

Figure 12 shows the MSD curves of bitumen in the different healing systems. It is clearly that there was a rapidly increasing period of MSD curves around 0-40 ps. In this period, the bitumen in the bitumen healing systems increased the most rapidly; then, the movements in the healing systems were gradually reduced around 40-150 ps when the reduction of bitumen healing systems was obviously less than that of other systems; another reduction period around 150-400 ps of the movements were followed with the less slope; finally the MSD would keep increment dynamically in the period of 400-1000 ps. Before 400 ps of simulated time, the MSD value followed the order that Fe_3O_4-a > Fe_2O_3-a > Fe_3O_4-a>bitumen> FeOOH-a> FeO-a> FeOOH-b> Fe_3O_4-b> Fe_2O_3-b> FeO-b. The above phenomena indicates that group-a possessed larger diffusion range than group-b and diffusion range of bitumen in the FeO healing systems was the narrowest in each group. It might be controlled by the combination of the attraction and appearance of iron corrosion products. After 400 ps of simulated time, diffusion range of bitumen in the FeOOH-a healing systems had a sudden increment and become the largest range.
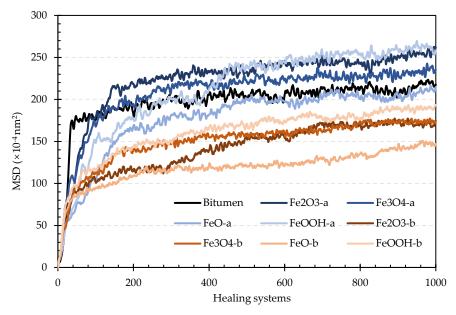
Figure 12 MSD curves of bitumen in the healing systems

According to the slope changing of MSD curves, the curves can be divided into four parts: 0-40 ps, 40-150 ps, 150-400 ps and 400-1000 ps. Commonly the diffusion coefficient could be only used for the equilibrium statement to obtain the diffusion characteristic of the material. In this section, diffusion coefficient was also used in the increment period to obtain the diffusion rate approximatively. Table 2 shows the diffusion coefficients of bitumen in the healing systems at different time periods. With the extension of time, the diffusion coefficients of bitumen in the healing systems would decrease rapidly at first and then slowly. It can be found that the movement rate in bitumen healing systems was the fast in the 0-40 ps. There were no obvious differences between the diffusion coefficients of group-a and group-b except 40-150 ps. In this period, the diffusion coefficients of group-a were obvious larger, indicating faster movement rate of bitumen molecules. Meanwhile, the movement of bitumen mainly focused on the diffusion on the surface of iron corrosion products in this period. This period should be considered the important period that could affect the healing degree.

The diffusion process was controlled by the interaction force inside the bitumen of the healing systems, which was changing with the acceleration linearly in the molecular dynamics based on Newton's second law. It can be defined as the second derivative of MSD^0.5 to the simulated time (T) accorded with dimension. It was also found that $\lg \frac{d\sqrt{MSD}}{dT}$ and lg T shows strong liner relationship, therefore the slope value of the relationship can represent the internal

488　force inside the bitumen in the healing systems. As shown in the Table 3, the value of R^2 have

489　proved the linear relationship. It can be observed that the internal force that motivated bitumen

490　molecules in the bitumen healing systems was the largest, and the internal force of group-a

491　were larger than that of group-b except FeOOH healing systems. The results also indicate that

492　Fe_3O_4 healing systems possess the largest internal force inside the bitumen in the iron corrosion

493　products systems.

494

495　　　　Table 2 Diffusion coefficients ($\times 10^{-4}$ nm²/ps) of bitumen in the healing systems

Healing systems	Time period			
	0-40 ps	40-150 ps	150-400 ps	400-1000 ps
Bitumen	0.863	0.022	0.009	0.003
Fe_2O_3-a	0.372	0.154	0.015	0.006
Fe_3O_4-a	0.517	0.133	0.021	0.004
FeO-a	0.268	0.133	0.019	0.005
FeOOH-a	0.315	0.131	0.025	0.010
Fe_2O_3-b	0.368	0.036	0.017	0.009
Fe_3O_4-b	0.358	0.055	0.014	0.006
FeO-b	0.362	0.024	0.010	0.008
FeOOH-b	0.419	0.053	0.018	0.007

496

497　　　Table 3 Evaluation of internal force motivating bitumen molecules in the healing systems

Healing systems	Relationships $(\lg \frac{d\sqrt{MSD}}{dT}$ - lg T)	R^2	Slope value
Bitumen	y = -2.0259x + 2.5933	R^2 = 0.9099	2.03
Fe_2O_3-a	y = -1.6323x + 1.9762	R^2 = 0.9512	1.63
Fe_3O_4-a	y = -1.8288x + 2.4216	R^2 = 0.9897	1.83
FeO-a	y = -1.5388x + 1.7244	R^2 = 0.9568	1.54
FeOOH-a	y = -1.3347x + 1.3952	R^2 = 0.975	1.34
Fe_2O_3-b	y = -1.3447x + 1.2406	R^2 = 0.9198	1.35
Fe_3O_4-b	y = -1.53x + 1.6271	R^2 = 0.9817	1.53
FeO-b	y = -1.3985x + 1.2431	R^2 = 0.8522	1.40
FeOOH-b	y = -1.5024x + 1.6233	R^2 = 0.9759	1.50

498

499　*4.4 Interaction effect in the healing systems*

500　　　Figure 13 demonstrates interaction evaluation in the healing systems. The interaction

501　energy of bitumen and bitumen, and Interaction energy of bitumen and iron corrosion products

502　were shown in Figure 13 (a) and (b) respectively. The interaction energy of bitumen and

503　bitumen in group-a was larger than that in group-b due to the distance difference. There was

504　insignificant regulation of the interaction energy of bitumen and bitumen between different

505　iron corrosion products. It was caused by that with the expansion of iron corrosion products,

506　the bitumen molecules that crossed the corrosion area were different, resulting in the

507　insignificant regularity. It can be observed that the interaction energy of bitumen and iron

508　corrosion products in group-b was larger than that in group-a caused by the larger volume and

509　contact surface. The interaction in the Fe_3O_4 healing systems was the most severe. The results

510　also indicate that the force by iron corrosion products should be regarded as the main power

511　that motivate the movement of bitumen molecules. It can be also found that the interaction

512　between bitumen and iron corrosion products was obviously larger than the interaction energy

513　of bitumen and bitumen. This difference would cause stress concentration easily in the

514　aggregation area on the iron corrosion product surface and generate weak areas. It indicates

515　that the main failure form should be cohesive failure once the cracks occurred again.

516　Meanwhile, the tearing on the sides of iron corrosion products between bitumen molecules was

517　accompanied. However, the accumulation of bitumen in the free area led to excessive internal

518　stress, which would make failure easier and weaken the healing effect. This can also be proved

519　by Figure 13 (c) and (d) where the debonding energy in the healing systems was quite larger

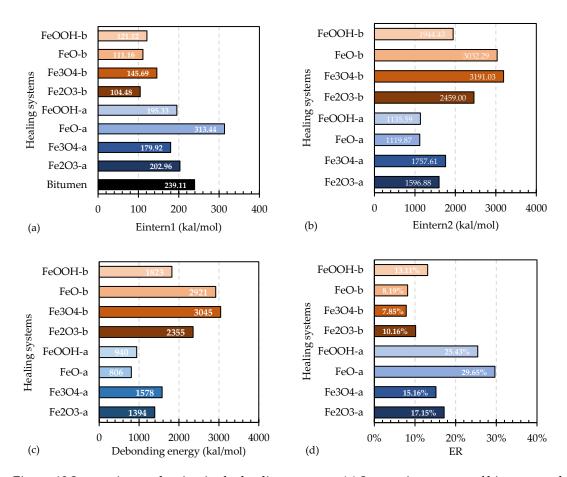520　than the interaction energy between bitumen and bitumen.

521

Figure 13 Interaction evaluation in the healing systems: (a) Interaction energy of bitumen and bitumen; (b) Interaction energy of bitumen and iron corrosion products; (c) Debonding energy; (d) ER

5   Conclusions

The investigation has been carried out to identify the influence of iron corrosion products on the healing process of bitumen by molecular dynamics simulation approach. Based on the results, the primary conclusions are as follows:

(1) The iron corrosion products have a dual effect on bitumen molecules: the attraction of iron corrosion products would make bitumen molecules climb to its surface to diffuse, while the products with larger volume would also reduce space of bitumen molecules movement and then obstruct the diffusion. The spatial structure of actual corrosion products is more complicated, and this dual effect may be affected.

(2) The iron corrosion products would result in the reduction of healing degree. Compared to other iron corrosion products, FeO healing systems had the best healing degree from in terms of crack closure and bitumen aggregation degree in the corrosion area

538   comprehensively, followed by Fe_3O_4, Fe_2O_3 and $FeOOH$.

539 (3) Diffusion coefficients of the period that bitumen molecules diffused on surface of iron

540   corrosion products were significantly different, which would make it vital in the healing

541   process. It was also related to the internal force and there is the largest internal force to

542   motivate bitumen molecules moving in the Fe_3O_4 healing systems.

543 (4) The interaction effect between bitumen and iron corrosion products is obviously larger

544   than the interaction effect between bitumen and bitumen. The difference would make more

545   bitumen molecules absorbed on the surface of the iron corrosion products where the

546   bitumen film would be thicker. It would result in cohesive failure becoming the main

547   failure form once the cracks re-occur.

548

549 **Author Contributions**: **Haiqin Xu**: Conceptualization, Methodology, Data curation, Writing-

550 Original draft, Writing - Review & Editing. **Yingxue Zou**: Methodology, Investigation, Writing

551 - Review & Editing. **Gordon Airey**: Investigation, Writing - Review & Editing. **Haopeng Wang**:

552 Methodology, Investigation, Data curation. **Hanyu Zhang**: Methodology, Investigation, Data

553 curation. **Shaopeng Wu**: Conceptualization, Funding acquisition, Supervision. **Anqi Chen**:

554 Conceptualization, Methodology, Project administration.

555

564

565 **Declaration of Competing Interest**: The authors declare that they have no known competing

566 financial interests or personal relationships that could have appeared to influence the work

567 reported in this paper.

568

Reference

[1] J. Xie, J. Chen, L. Hu, S. Wu, Z. Wang, M. Li, C. Yang, Preparation, thermochromic properties and temperature controlling ability of novel pellets in ultra-thin wearing course, Constr. Build. Mater. 389 (2023) 131797. https://doi.org/10.1016/j.conbuildmat.2023.131797.

[2] C. Yang, S. Wu, P. Cui, S. Amirkhanian, Z. Zhao, F. Wang, L. Zhang, M. Wei, X. Zhou, J. Xie, Performance characterization and enhancement mechanism of recycled asphalt mixtures involving high RAP content and steel slag, J. Clean. Prod. 336 (2022) 130484. https://doi.org/10.1016/j.jclepro.2022.130484.

[3] P. Cui, S. Wu, Y. Xiao, R. Hu, T. Yang, Environmental performance and functional analysis of chip seals with recycled basic oxygen furnace slag as aggregate, J. Hazard. Mater. 405 (2021) 124441. https://doi.org/10.1016/j.jhazmat.2020.124441.

[4] European Commission. Directorate General for Regional and Urban Policy., Road infrastructure in Europe: road length and its impact on road performance., Publications Office, LU, 2022. https://data.europa.eu/doi/10.2776/21558 (accessed June 21, 2023).

[5] European Union Road Federation (ERF), Road Asset Management: An ERF Position Paper for Maintaining and Improving a Sustainable and Efficient Road Network, (2014). https://trid.trb.org/view/1357497 (accessed June 21, 2023).

[6] H. Xu, S. Wu, A. Chen, Y. Zou, C. Yang, P. Cui, Study on preparation and characterization of a functional porous ultra-thin friction course (PUFC) with recycled steel slag as aggregate, J. Clean. Prod. 380 (2022) 134983. https://doi.org/10.1016/j.jclepro.2022.134983.

[7] Y. Zou, S. Amirkhanian, S. Xu, Y. Li, Y. Wang, J. Zhang, Effect of different aqueous solutions on physicochemical properties of asphalt binder, Constr. Build. Mater. 286 (2021) 122810. https://doi.org/10.1016/j.conbuildmat.2021.122810.

[8] Y. Li, H. Li, S. Nie, S. Wu, Q. Liu, C. Li, B. Shu, C. Li, W. Song, Y. zou, L. Pang, Negative impacts of environmental factors (UV radiation, water and different solutions) on bitumen and its mechanism, Constr. Build. Mater. 265 (2020). https://doi.org/10.1016/j.conbuildmat.2020.120288.

[9] Z. Zhao, S. Wu, J. Xie, C. Yang, F. Wang, N. Li, Q. Liu, S. Amirkhanian, Effect of direct addition of asphalt rubber pellets on mixing, performance and VOCs of asphalt mixtures, Constr. Build. Mater. 411 (2024) 134494. https://doi.org/10.1016/j.conbuildmat.2023.134494.

[10] Y. Zou, H. Xu, S. Xu, A. Chen, S. Wu, S. Amirkhanian, P. Wan, X. Gao, Investigation of the moisture damage and the erosion depth on asphalt, Constr. Build. Mater. 369 (2023) 130503. https://doi.org/10.1016/j.conbuildmat.2023.130503.

[11] H. Yang, L. Pang, Y. Zou, Q. Liu, J. Xie, The effect of water solution erosion on rheological, cohesion and adhesion properties of asphalt, Constr. Build. Mater. 246 (2020) 118465. https://doi.org/10.1016/j.conbuildmat.2020.118465.

[12] Ministry of Transport of the People's Republic of China, Statistical Bulletin on the Development of Transportation Industry in 2022, (2023). https://xxgk.mot.gov.cn/2020/jigou/zhghs/202306/t20230615_3847023.html (accessed June 17, 2023).

[13] F. Zhao, Q. Liu, Z. Peng, H. Wang, P. Wan, Q. Ye, A comparative study of the effects of calcium alginate capsules on self-healing properties of base and SBS modified asphalt mixtures, Constr. Build. Mater. 364 (2023). https://doi.org/10.1016/j.conbuildmat.2022.129908.

[14] Y. Sun, L. Zheng, Y. Cheng, F. Chi, K. Liu, T. Zhu, Research on maintenance equipment and maintenance technology of steel fiber modified asphalt pavement with microwave heating, Case Stud. Constr. Mater. 18 (2023) e01965. https://doi.org/10.1016/j.cscm.2023.e01965.

[15] C. Fu, F. Wang, K. Liu, Q. Liu, P. Liu, M. Oeser, Inductive asphalt pavement layers for improving electromagnetic heating performance, Int. J. Pavement Eng. 24 (2023) 2159401. https://doi.org/10.1080/10298436.2022.2159401.

[16] E. Yalcin, Effects of microwave and induction heating on the mechanical and self-healing characteristics of the asphalt mixtures containing waste metal, Constr. Build. Mater. 286 (2021). https://doi.org/10.1016/j.conbuildmat.2021.122965.

[17] C. Yang, S. Wu, J. Xie, S. Amirkhanian, Z. Zhao, H. Xu, F. Wang, L. Zhang, Development of blending model for RAP and virgin asphalt in recycled asphalt mixtures via a micron-Fe3O4 tracer, J. Clean. Prod. 383 (2023) 135407. https://doi.org/10.1016/j.jclepro.2022.135407.

[18] K. Liu, C. Fu, P. Xu, S. Li, M. Huang, An eco-friendliness inductive asphalt mixture comprising waste steel shavings and waste ferrites, J. Clean. Prod. 283 (2021). https://doi.org/10.1016/j.jclepro.2020.124639.

[19] M.M. Karimi, M.K. Darabi, J.F. Rushing, B.C. Cox, Coupled Thermo-Electromagnetic microstructural modeling of inductive aggregate blends, Constr. Build. Mater. 302 (2021). https://doi.org/10.1016/j.conbuildmat.2021.124107.

[20] Wang, Wu, Li, Xu, Xu, Shi, Wang, Microscopic Analysis of Steel Corrosion Products in Seawater and Sea-Sand Concrete, Materials 12 (2019) 3330. https://doi.org/10.3390/ma12203330.

[21] G.S. Duffó, W. Morris, I. Raspini, C. Saragovi, A study of steel rebars embedded in concrete during 65 years, Corros. Sci. 46 (2004) 2143–2157. https://doi.org/10.1016/j.corsci.2004.01.006.

[22] K. Suda, S. Misra, K. Motohashi, Corrosion Products of Reinforcing Bars Embedded in Concrete, Corros. Sci. 35 (1993) 1543–1549. https://doi.org/10.1016/0010-938X(93)90382-Q.

[23] H. Li, J. Yu, S. Wu, Q. Liu, Y. Wu, H. Xu, Y. Li, Effect of moisture conditioning on mechanical and healing properties of inductive asphalt concrete, Constr. Build. Mater. 241 (2020). https://doi.org/10.1016/j.conbuildmat.2020.118139.

[24] H. Xu, S. Wu, A. Chen, Y. Zou, Influence of erosion factors (time, depths and environment) on induction heating asphalt concrete and its mechanism, J. Clean. Prod. 363 (2022) 132521. https://doi.org/10.1016/j.jclepro.2022.132521.

[25] S. Sanyal, R. Chelliah, T. Kim, M. Rabelo, D.-H. Oh, D.P. Pham, J. Yi, Crack resistance of a noble green hydrophobic antimicrobial sealing coating film against environmental corrosion applied on the steel–cement interface for power insulators, RSC Adv. 12 (2022) 10126–10141. https://doi.org/10.1039/D2RA00747A.

[26] LAMMPS Molecular Dynamics Simulator, (n.d.). https://www.lammps.org/ (accessed January 8, 2024).

[27]   H. A, Z. Yang, R. Hu, Y.-F. Chen, L. Yang, Effect of Solid–Liquid Interactions on Substrate Wettability and Dynamic Spreading of Nanodroplets: A Molecular Dynamics Study, J. Phys. Chem. C 124 (2020) 23260–23269. https://doi.org/10.1021/acs.jpcc.0c07919.

[28]   M. Benhassine, E. Saiz, A.P. Tomsia, J. De Coninck, Nonreactive wetting kinetics of binary alloys: A molecular dynamics study, Acta Mater. 59 (2011) 1087–1094. https://doi.org/10.1016/j.actamat.2010.10.039.

[29]   Z. Du, X. Zhu, Molecular Dynamics Simulation to Investigate the Adhesion and Diffusion of Asphalt Binder on Aggregate Surfaces, Transp. Res. Rec. 2673 (2019) 500–512. https://doi.org/10.1177/0361198119837223.

[30]   J. Xu, B. Ma, W. Mao, W. Si, X. Wang, Review of interfacial adhesion between asphalt and aggregate based on molecular dynamics, Constr. Build. Mater. 362 (2023). https://doi.org/10.1016/j.conbuildmat.2022.129642.

[31]   H. Xu, Y. Zou, G. Airey, H. Wang, H. Zhang, S. Wu, A. Chen, Wetting of bio-rejuvenator nanodroplets on bitumen: A molecular dynamics investigation, J. Clean. Prod. (2024) 141140. https://doi.org/10.1016/j.jclepro.2024.141140.

[32]   A. Bhasin, R. Bommavaram, M.L. Greenfield, D.N. Little, Use of Molecular Dynamics to Investigate Self-Healing Mechanisms in Asphalt Binders, J. Mater. Civ. Eng. 23 (2011) 485–492.

[33]   D. Sun, T. Lin, X. Zhu, Y. Tian, F. Liu, Indices for self-healing performance assessments based on molecular dynamics simulation of asphalt binders, Comput. Mater. Sci. 114 (2016) 86–93. https://doi.org/10.1016/j.commatsci.2015.12.017.

[34]   D. Sun, G. Sun, X. Zhu, F. Ye, J. Xu, Intrinsic temperature sensitive self-healing character of asphalt binders based on molecular dynamics simulations, Fuel 211 (2018) 609–620. https://doi.org/10.1016/j.fuel.2017.09.089.

[35]   X. Qu, D. Wang, Y. Hou, M. Oeser, L. Wang, Influence of Paraffin on the Microproperties of Asphalt Binder Using MD Simulation, J. Mater. Civ. Eng. 30 (2018). https://doi.org/10.1061/(ASCE)MT.1943-5533.0002368.

[36]   H. Zhang, Q. Zhang, M. Li, T. Yu, Behavior Characteristics of Asphalt Components during the Process of Nano-cracks Temperature Self-healing, J. Wuhan Univ. Technol.-Mater Sci Ed 38 (2023) 149–155. https://doi.org/10.1007/s11595-023-2677-9.

[37]   N. Xu, H. Wang, Y. Chen, N. Hossiney, Z. Ma, H. Wang, Insight into the effects of waste vegetable oil on self-healing behavior of bitumen binder, Constr. Build. Mater. 363 (2023) 129888. https://doi.org/10.1016/j.conbuildmat.2022.129888.

[38]   X. Zhang, X. Zhou, F. Zhang, W. Ji, F. Otto, Study of the self-healing properties of aged asphalt-binder regenerated using residual soybean-oil, J. Appl. Polym. Sci. 139 (2022). https://doi.org/10.1002/app.51523.

[39]   F. Nie, W. Jian, D. Lau, Advanced Self-Healing Asphalt Reinforced by Graphene Structures: An Atomistic Insight, J. Vis. Exp. (2022) 63303. https://doi.org/10.3791/63303.

[40]   M. Li, S. Li, C. Zhu, N. Li, H. Wang, Effect of Iron Oxide on Self-Healing and Thermal Characteristics of Asphalt Based on Molecular Dynamics Simulation Perspective, Adv. Mater. Sci. Eng. 2022 (2022) 1–14. https://doi.org/10.1155/2022/7931571.

[41]   Y. Gong, J. Xu, E. Yan, J. Cai, The Self-Healing Performance of Carbon-Based Nanomaterials Modified Asphalt Binders Based on Molecular Dynamics Simulations, Front. Mater. 7 (2021). https://doi.org/10.3389/fmats.2020.599551.

[42] D. Hu, J. Pei, R. Li, J. Zhang, Y. Jia, Z. Fan, Using thermodynamic parameters to study self-healing and interface properties of crumb rubber modified asphalt based on molecular dynamics simulation, Front. Struct. Civ. Eng. 14 (2020) 109–122. https://doi.org/10.1007/s11709-019-0579-6.

[43] M. Guo, Y. Tan, L. Wang, Y. Hou, Diffusion of asphaltene, resin, aromatic and saturate components of asphalt on mineral aggregates surface: molecular dynamics simulation, ROAD Mater. PAVEMENT Des. 18 (2017) 149–158. https://doi.org/10.1080/14680629.2017.1329870.

[44] G. Sun, Z. Niu, J. Zhang, X. Tan, Y. Jing, Z. Chen, Impacts of asphalt and mineral types on interfacial behaviors: A molecular dynamics study, CASE Stud. Constr. Mater. 17 (2022). https://doi.org/10.1016/j.cscm.2022.e01581.

[45] D.D. Li, M.L. Greenfield, Chemical compositions of improved model asphalt systems for molecular simulations, Fuel 115 (2014) 347–356. https://doi.org/10.1016/j.fuel.2013.07.012.

[46] C. Zheng, C. Shan, J. Liu, T. Zhang, X. Yang, D. Lv, Microscopic adhesion properties of asphalt-mineral aggregate interface in cold area based on molecular simulation technology, Constr. Build. Mater. 268 (2021). https://doi.org/10.1016/j.conbuildmat.2020.121151.

[47] Y. Zou, Y. Gao, A. Chen, S. Wu, Y. Li, H. Xu, H. Wang, Y. Yang, S. Amirkhanian, Adhesion failure mechanism of asphalt-aggregate interface under an extreme saline environment: A molecular dynamics study, Appl. Surf. Sci. (2023) 158851. https://doi.org/10.1016/j.apsusc.2023.158851.

[48] N.H. de Leeuw, T.G. Cooper, Surface simulation studies of the hydration of white rust Fe(OH)2, goethite α-FeO(OH) and hematite α-Fe2O3, Geochim. Cosmochim. Acta 71 (2007) 1655–1673. https://doi.org/10.1016/j.gca.2007.01.002.

[49] E. Zepeda-Alarcon, H. Nakotte, A.F. Gualtieri, G. King, K. Page, S.C. Vogel, H.-W. Wang, H.-R. Wenk, Magnetic and nuclear structure of goethite (α-FeOOH): a neutron diffraction study, J. Appl. Crystallogr. 47 (2014) 1983–1991. https://doi.org/10.1107/S1600576714022651.

[50] M. Valášková, J. Tokarský, J. Pavlovský, T. Prostějovský, K. Kočí, α-Fe2O3 Nanoparticles/Vermiculite Clay Material: Structural, Optical and Photocatalytic Properties, Materials 12 (2019) 1880. https://doi.org/10.3390/ma12111880.

[51] W.A. Bassett, L.-G. Liu, Experimental determination of the effects of pressure and temperature on the stoichiometry and phase relations of wiistite, (n.d.).

[52] M.H.N. Assadi, J.J. Gutiérrez Moreno, D.A.H. Hanaor, H. Katayama-Yoshida, Exceptionally high saturation magnetisation in Eu-doped magnetite stabilised by spin–orbit interaction, Phys. Chem. Chem. Phys. 23 (n.d.) 20129–20137. https://doi.org/10.1039/D1CP02164H.

[53] G. Bahlakeh, M. Ghaffari, M.R. Saeb, B. Ramezanzadeh, F. De Proft, H. Terryn, A Close-up of the Effect of Iron Oxide Type on the Interfacial Interaction between Epoxy and Carbon Steel: Combined Molecular Dynamics Simulations and Quantum Mechanics, J. Phys. Chem. C 120 (2016) 11014–11026. https://doi.org/10.1021/acs.jpcc.6b03133.

[54] S.S. Rath, N. Sinha, H. Sahoo, B. Das, B.K. Mishra, Molecular modeling studies of oleate adsorption on iron oxides, Appl. Surf. Sci. 295 (2014) 115–122. https://doi.org/10.1016/j.apsusc.2014.01.014.

743   [55]   W.A. Deer, R.A. Howie, J. Zussman, An Introduction to the Rock-Forming Minerals,
744   (2013). https://doi.org/10.1180/DHZ.
745   [56]   F. Guo, J. Pei, G. Huang, J. Zhang, A. Falchetto, L. Korkiala-Tanttu, Investigation of the
746   adhesion and debonding behaviors of rubber asphalt and aggregates using molecular
747   dynamics   simulation,   Constr.   Build.   Mater.   371   (2023).
748   https://doi.org/10.1016/j.conbuildmat.2023.130781.
749